Journal of CO2 Utilization 111 (2026) 103543

Contents lists available at ScienceDirect

Journal of CO2 Utilization

journal homepage: www.elsevier.com/locate/jcou

Role of potassium on reaction pathways in CO_2 hydrogenation: Insights from reverse water gas shift and Fischer-Tropsch synthesis over the carbon-supported iron-based catalysts

Weixin Meng [a], Renske Rocks [a], A. Iulian Dugulan [b], Jingxiu Xie [a,*]

[a] Green Chemical Reaction Engineering, Engineering and Technology Institute Groningen, University of Groningen, Nijenborgh 3, Groningen 9747 AG, the Netherlands
[b] Laboratory of Fundamentals Aspects of Materials and Energy, Department of Radiation Science & Technology, Delft University of Technology, Mekelweg 15, Delft 2628 CD, the Netherlands

ARTICLE INFO

Keywords:
CO_2 hydrogenation
RWGS
FTS
Fe carbides
K promotion

ABSTRACT

Potassium (K) has been widely employed as an alkali promoter for Fe-based catalysts in the reverse water gas shift (RWGS) reaction, Fischer-Trospch synthesis (FTS) and the integration of RWGS and FTS for direct CO_2 hydrogenation to higher hydrocarbons, commonly referred to as the CO_2-FTS process. K is recognized as both a structural promoter of the Fe phase and an electronic promoter that modifies the adsorption and activation behavior of reactants on the catalyst surface. However, its role in reaction pathways and the effect of K loading in each reaction remains largely unexplored. In this study, a series of K-promoted carbon-supported Fe-based catalysts was prepared to investigate the effect of K/Fe molar ratios from 0.02 to 0.5 on the RWGS and FTS reactions in a fixed-bed reactor at 300 °C, 11 bar, $H_2/CO_2/Ar$=3/1/1, 1000–375000 $mL \cdot g_{cat}^{-1} \cdot h^{-1}$. Quasi in situ Mössbauer spectroscopy shows that sufficient K promotion (K/Fe $\geq$ 0.1) on carbon-supported Fe-based catalysts led to complete carburization following a reduction-carburization activation procedure. The resulting Fe carbides remained stable after both RWGS and FTS conditions, suggesting that they are responsible for catalyzing both reactions. This finding contrasts with literature reports that attribute RWGS and FTS activity to Fe oxides and Fe carbides, respectively. Increasing the K/Fe ratio progressively suppressed CO_2 methanation as a primary reaction, ultimately rendering primary methanation insignificant and leaving RWGS as the only primary reaction. Both RWGS and FTS activities reached their optimum at a K/Fe ratio of 0.1. However, a higher K/Fe ratio led to higher CO selectivity in the RWGS reaction, whereas an optimal K/Fe ratio of 0.1 was found for FTS to promote the production of higher hydrocarbons.

1. Introduction

CO_2 capture and utilization is considered a promising strategy for reducing CO_2 emissions while producing synthetic chemicals and fuels. [1,2] However, CO_2 is a thermodynamically stable molecule and must first be activated into more reactive C_1 molecules, such as CO and methanol. [3,4] The reverse water gas shift (RWGS) reaction converts CO_2 to CO, which is subsequently hydrogenated to form C_{2+} hydrocarbons via Fischer-Trospch synethesis (FTS). The integration of these consecutive pathways enables a direct CO_2-FTS process. [5–8] Fe-based catalysts are active and selective for both RWGS and CO-FTS reactions, with Fe_3O_4 and Fe_5C_2 identified in literature as the active phases, respectively. [9–14] However, in additional to the desired pathways, Fe-based catalysts also suffer from competing side reactions, such as CO_2 methanation (Sabatier reaction) and CO methanation, resulting in methane formation and pose a significant challenge in achieving high selectivity toward C_{2+} hydrocarbons. [15,16]

The addition of alkali metal promotes CO_2 conversion, suppresses CH_4 formation, and improves the selectivity toward long-chain hydrocarbons during the CO_2-FTS. [17–22]. Potassium (K) is the most frequently used promoter in Fe-based catalysts to improve the performance of both RWGS and CO-FTS reactions. [23–26] Previous investigations have primarily focused on elucidating its effects as a structural promoter of the Fe phase and as an electronic promoter influencing the adsorption and activation of reactants on the catalyst surface. [27–32] The addition of K to Fe-based RWGS catalysts has been

* Corresponding author.
E-mail address: jingxiu.xie@rug.nl (J. Xie).

https://doi.org/10.1016/j.jcou.2026.103543
Received 5 May 2026; Received in revised form 26 July 2026; Accepted 11 August 2026
Available online 17 August 2026

used to strengthen CO_2 adsorption and activation by increasing electron density on Fe atoms, as well as the reaction mechanism. [27,33–38]. Loiland et al. reported that K addition to Fe/γ-Al_2O_3 (Fe/K mass ratio=1.24) led to a threefold increase in CO formation rates at 480 °C, 1 bar, H_2/CO=1. Under differential conditions, CO_2 conversion remained below 10% while CO selectivity exceeded 99% for both catalysts. The results suggest that both redox and associative mechanisms occur over the Fe-K/γ-Al_2O_3 whereas only the redox mechanism is present over the unpromoted catalyst. [39] This finding is further supported by DFT calculated performed Tian et al. who demonstrated that K_2O increases surface basicity of Fe_3O_4, thereby shifting the reaction pathway from the redox to the associative mechanism and promoting CO_2 activation. [40] In addition, the incorporation of K has been widely reported to enhance the RWGS rate. [41] Amoyal et al. demonstrated that 2 wt% K in Fe-Al-O spinel catalysts increased the RWGS rate tenfold compared with the unpromoted oxide at 350 °C, 20 bar, $H_2/CO_2/H_2O$=0.6/0.2/0.2. This improvement was correlated with the increase of Fe^{2+}/Fe^{3+} ratio and a higher oxygen vacancies as active sites for RWGS. [42] Utsis et al. observed that an optimal K loading of 6 wt% in BaFe-hexaaluminates catalyst increased the RWGS rates by a factor of 12–15, which was attributed to higher concentration of active sites, associated with the reduction of Fe^{3+} to Fe^{2+} by K as the reducing agent. [43]

K has also been extensively studied for its role in enhancing FTS activity and chain growth probability. [44–47] These promotional effects are generally attributed to its ability to strengthen CO dissociative adsorption, inhibit H_2 adsorption, promote C-C coupling, increase catalyst basicity, and facilitate the formation of Fe carbides. [31,48,49] FTS performance typically displays a maximum at intermediate K loadings, [47,50–52] as excessive K can block the active sites and favor the carbon deposition on the surface. [51,53] For instance, Yang et al. reported that FTS activity over the Fe/Mn catalysts reached a maximum at 0.7 wt% K within the examined range of 0–3.0 wt% at 250–320 °C, 25 bar, H_2/CO=2. Beyond this optimal loading, a pronounced decline in catalytic activity was observed, which was attributed to suppressed H_2 chemisorption and enhanced CO chemisorption, ultimately leading to the carbon deposition on the surface. [51] Tian et al. observed that, within the investigated K range of 0–5 wt%, catalytic activity (320 °C, 20 bar, H_2/CO=1) over the Fe_3C@C catalyst declined above 1 wt% K due to excessive K promoting the growth of χ-Fe_5C_2 and reducing the active sites, whereas the highest olefin selectivity (41.9%) was achieved over the 2K-Fe_3C@C catalyst (2 wt% K). [52]

Considerable efforts have also been devoted to varying K loading for Fe-based CO_2-FTS catalysts. [54–58] Figs. 1 and 2 (data included in Table S1) illustrate the state-of-the-art performance of CO_2-FTS with respect to K addition to bulk and supported Fe-based catalysts respectively. From Fig. 1, bulk Fe-based catalysts without K promotion show lower CO and C_{2+} hydrocarbon selectivities and higher CH_4 selectivity in comparison to their counterparts with K promotion. Extrapolating the selectivity towards zero CO_2 conversion allows identification of primary reactions, and the unpromoted Fe-based catalysts (0AM/Fe, Fe and Fe_5C_2) show primary RWGS and CO_2 methanation. The K-promoted Fe-based catalysts show a clear suppression of methanation, although primary RWGS and CO_2 methanation still occurred except for K (4)-Fe_5C_2 which has RWGS as the only primary reaction. The variation in K loading on bulk Fe_2O_3 catalysts from 0.001 K/Fe to 0.05 K/Fe does not appear to affect product selectivity and reaction pathways, as reported by Yang et al., as both RWGS and CO_2 methanation occur in parallel regardless of K loading. [27] Interestingly, the Fe-K catalyst shows primary RWGS, CO_2 methanation and FTS, as evidenced by the CO, CH_4 and C_{2+} hydrocarbon product observed at close to zero CO_2 conversion. [59] The various reaction pathways are illustrated in Fig. 3. From Fig. 2, most reported datasets on K addition to supported Fe-based catalysts employ oxide supports, while our previous work focuses on carbon-supported catalysts. [60] The general findings from bulk Fe-based catalysts regarding K promotion, such as the suppression of CH_4 selectivity and the identification of three main reaction mechanisms, are also applicable to supported catalysts. Notably, there is no consensus on the effect of the K loading on the reaction pathway and the product selectivity-CO_2 conversion relationship.

The aim of this study is to investigate the effect of K on reaction pathways in the CO_2 hydrogenation over carbon-supported Fe-based catalysts, with particular emphasis on primary RWGS and secondary FTS reactions. The Fe loading was fixed at 15 wt% while the K loading was varied from 0.2 to 3.8 wt%, resulting in K/Fe molar ratios ranging from 0.02 to 0.5. The Fe loading was selected to achieve an average nanoparticle size of 9 nm, which lies outside the particle size effect (structure sensitivity) prominent for nanoparticle sizes from 1 to 10 nm. [60–63] After activation, the catalysts were evaluated at 300 °C, 11 bar, $H_2/CO_2/Ar$=3/1/1, 1000–375000 $mL \cdot g_{cat}^{-1} \cdot h^{-1}$. Space velocities were adjusted to achieve the complete range of CO_2 conversions, reaching the CO_2-FTS threshold of 38%. Primary reactions were identified by extrapolating product selectivities towards zero CO_2 conversions. As RWGS and FTS are primary and secondary reaction pathways, the influence of K on RWGS was evaluated at a CO_2 conversion of ~7%, and its effect on FTS was assessed at ~33% CO_2 conversion. Quasi in situ Mössbauer spectroscopy was used to identify and quantify Fe phases during reduction, carburization, RWGS, and FTS, providing insights into the influence of K on Fe phases and the resulting structure-performance relationships.

2. Experimental methods

2.1. Catalyst preparation

The carbon-supported Fe-based catalysts with a fixed Fe loading of

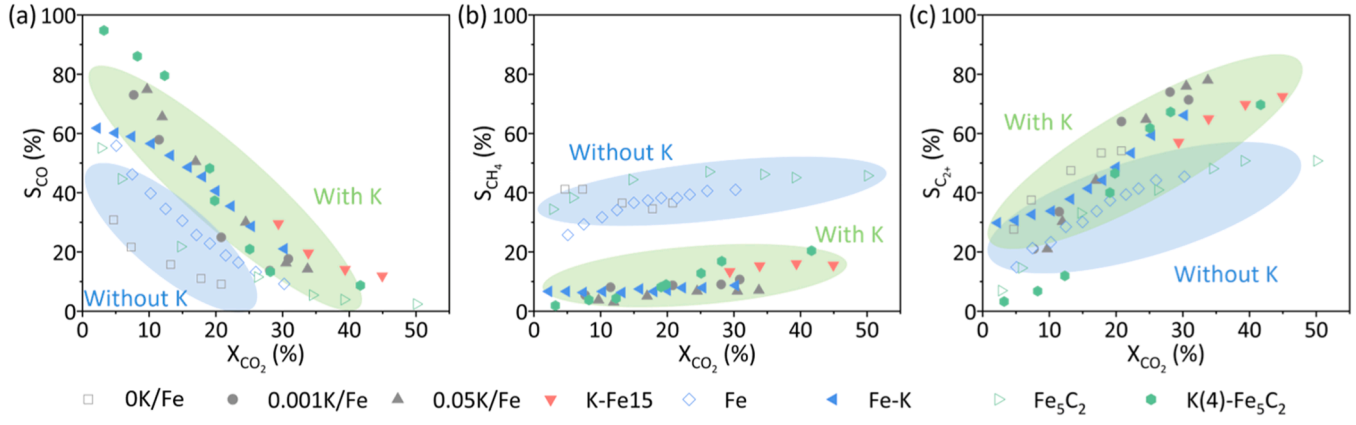

Fig. 1. Product selectivity-CO_2 conversion relationship over the bulk Fe-based catalysts with or without K.

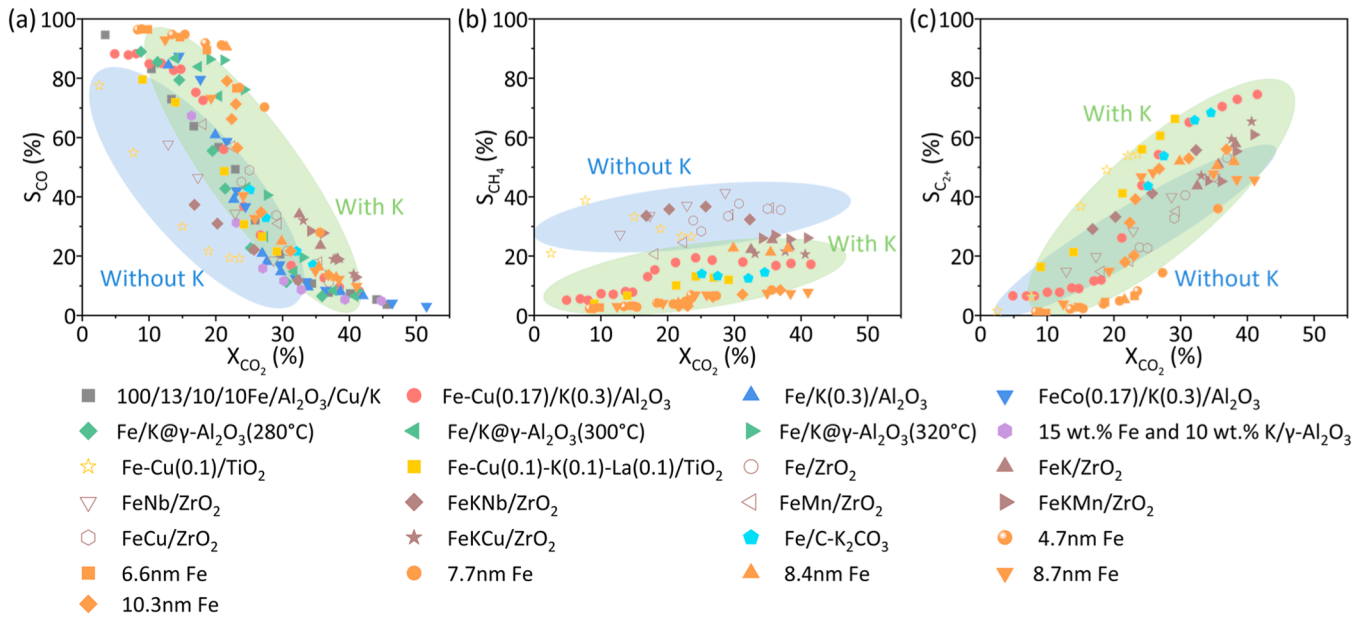

Fig. 2. Product selectivity-CO_2 conversion relationship over the supported Fe-based catalysts with or without K.

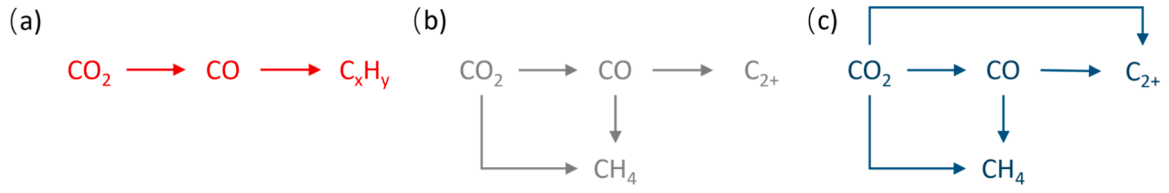

Fig. 3. Reaction pathways of CO_2 hydrogenation via RWGS and FTS.

15 wt% and various K loadings were prepared via the incipient wetness impregnation method. The K to Fe molar ratios were varied from 0.02 to 0.5, and the corresponding samples were denoted as K/Fe_x (x=0.02, 0.05, 0.1, 0.25 and 0.5). A Fe-only catalyst without K was referred to as bare Fe. Typically, ammonium iron citrate (Sigma-Aldrich, 16.5–18.5 wt% Fe) and potassium nitrate (Sigma-Aldrich, ≥ 99.0%) were dissolved in deionized water, followed by the addition of methanol at an H_2O-to-MeOH volume ratio of 2:1. The solubility of the ammonium iron citrate precursor was 1 g/mL in deionized water. The obtained precursor solution was injected to saturate the pore volume (measured by N_2 physisorption) of carbon support (Cabot, VXC 72, 100%, 75–150 μm). Due to limited pore volume, multiple impregnation steps were required. Between each successive impregnation step, the sample was dried under static air at 110 °C for 1 h. After the final impregnation, the sample was dried overnight. The catalyst was then subjected to heat treatment at 500 °C (2 °C·min^{-1}) for 2 h under N_2 flow.

2.2. Characterization

The metal loadings were determined by the thermogravimetric analysis (TGA) using a Perkin Elmer TGA 4000. The samples were loaded into a crucible and heated from 50 to 750 °C (5 °C·min^{-1}) under the airflow (25 mL·min^{-1}). The elemental compositions of samples were analyzed by X-ray fluorescence (XRF) using a Malvern Panalytical Epsilon3^{XLE}. The Fe and K loadings were calculated by combining the data obtained from TGA and XRF measurements, with TGA providing total Fe and K loading and XRF determining the Fe/K distribution.

Textural properties of the samples, including surface area, pore volume, and pore size distribution, were analyzed by N_2 adsorption-desorption isotherm measurement using a Micromeritics ASAP 2420 analyzer. Prior to analysis, the samples were degassed under vacuum at 200 °C for 12 h to remove adsorbed gases and moisture. The specific surface area was calculated using the Brunauer-Emmett-Teller (BET) method. The pore volume was estimated from the single-point desorption data at P/P°=0.99. The pore size was obtained from the desorption branch using the Barrett-Joyner-Halenda (BJH) method.

The crystal structure and phase composition of samples were analyzed by X-ray diffraction (XRD) using a Bruker D8 Endeavor diffractometer operated at 40 kV and 25 mA with Cu-Kα radiation (λ=1.5418 Å). Diffraction patterns were collected over a 2θ range of 20° to 90° with a step size of 0.02° and a step time of 1 s.

The average size and distribution of Fe nanoparticles were determined by transmission electron microscopy (TEM) using a Philips CM120 microscope operated at 120 kV. The sample was ultrasonically dispersed in ethanol for 5 min, then deposited on a carbon-coated Cu grid and dried for a few minutes. At least 300 nanoparticles were measured to calculate the average size and distribution.

Catalyst reducibility was measured by H_2-Temperature Programmed Reduction (H_2-TPR) using the AutoChem II 2920 automatic chemical adsorption instrument. 0.1 g of the sample was loaded in a U-shaped tube and first purged with helium at 150 °C for 60 min. The sample was then cooled to 50 °C, and the flow was switched to 5% H_2 in Ar gas. The sample was heated from 50 to 600 °C with a heating rate of 5 °C·min^{-1}. The H_2 consumption signal was detected by the thermal conductivity detector (TCD).

The evolution of the Fe phase was measured by Mössbauer spectroscopy. The experiments were conducted using a high-pressure quasi in situ Mössbauer cell - developed at Reactor Institute Delft. The high-pressure beryllium windows used in this cell contain 0.08% Fe impurity, whose spectral contribution was fitted and removed from the final spectra. Transmission ^{57}Fe Mössbauer spectra were recorded at 4.2 K using a conventional constant-acceleration spectrometer with a ^{57}Co

(Rh) source. Measurements at 120 K were performed with a sinusoidal velocity spectrometer, in which the source and the absorbing samples were kept at the same temperature. Velocity calibration was carried out using an α-Fe foil at room temperature. The Mössbauer spectra were fitted using the Mosswinn 4.0 program. 70 or 200 mg of catalyst was loaded to the cell. Reduction and carburization conditions were identical to those used for the catalytic performance testing in section 2.3. To achieve a lower conversion, the experimental condition was conducted at 300 °C, 11 bar, $H_2/CO_2/Ar$=3/1/1, 49500 mL·g_{cat}^{-1}·h^{-1} for bare Fe and K/Fe_0.5, while 141428 mL·g_{cat}^{-1}·h^{-1} for K/Fe_0.1. For higher conversion, 3000 mL·g_{cat}^{-1}·h^{-1} was applied to all catalysts.

2.3. Catalytic Performance Testing

Catalytic experiments were conducted in a stainless-steel fixed-bed reactor setup (Microactivity Effi, PID Eng). Carbon-supported Fe-based catalysts (75–150 μm) were diluted with SiC (25–75 μm). Prior to the CO_2 hydrogenation reaction, the catalyst was first reduced in H_2/Ar (1/1) at 400 °C (5 °C·min^{-1}), 2 bar for 2 h, followed by carburization with H_2/CO/Ar (2/2/1) at 280 °C, 2 bar for 20 h. The reaction was then carried out at 300 °C, 11 bar, $H_2/CO_2/Ar$=3/1/1, 1000–375000 mL·g_{cat}^{-1}·h^{-1}. A blank run with only C support and SiC was also performed at 300 °C, 11 bar, $H_2/CO_2/Ar$=3/1/1, 3000 mL·g_{cat}^{-1}·h^{-1} to rule out thermal and support-mediated CO_2 conversion (Figure S1). The catalytic data were obtained from steady-state measurements at different GHSVs and each data point was recorded after stabilization of CO_2 conversion and product selectivity (Figures S2-S7). To further verify catalyst stability, a representative condition under identical GHSV was repeated at the end of each experimental sequence. Full set of conditions and corresponding catalytic data can be found in Supporting Table S2. The product selectivity was analyzed online using a gas chromatography analyser, Thermo TraceGC 1310, equipped with one thermal conductivity detector (TCD) and two flame ionization detectors (FID). The TCD channel, equipped with ShinCarbon ST and Hayesep Q columns and a TCD, was used for the analysis of the permanent gases. The first FID channel, equipped with a GS-gaspro column and a FID, was used to quantify C_1 to C_9 hydrocarbons. The second FID channel, equipped with a Stabilwax column and a FID, was used to detect and measure oxygenates and aromatics. No oxygen-containing or aromatic-containing products were detected. Carbon balance was between 87% and 106%.

The residence time was calculated by Eq. 1. CO_2 conversion was calculated according to Eq. 2. Product selectivity toward CO and hydrocarbons containing up to nine carbon atoms (C_9) was calculated according to Eq. 3. The ratio of primary reaction rates (RWGS and CO_2 methanation) was calculated according to Eq. 4. The formation rates of the products were calculated based on the Fe time yield (FTY) according to Eq. 5.

$$\tau = \frac{V}{Q} * 60 \tag{1}$$

$$X_{CO_2} = \frac{CO_{2,\ in} - \frac{Ar_{in}}{Ar_{out}} * CO_{2,\ out}}{CO_{2,\ in}} * 100\% \tag{2}$$

$$S_{product} = \frac{\frac{Ar_{in}}{Ar_{out}} * product_{out} * n}{CO_{2,\ in} - \frac{Ar_{in}}{Ar_{out}} * CO_{2,\ out}} * 100\% \tag{3}$$

$$\frac{r_{CH_4,\ p}}{r_{RWGS,\ p}} = \frac{S_{CH_4,\ p}}{S_{CO,\ p}} \tag{4}$$

$$FTY_{product} = \frac{GHSV * m_{CO_2,\ in} * X_{CO_2} * S_{product}}{W_{Fe} * V_m} \tag{5}$$

Where V is the volume of catalyst (mL) and Q is the volumetric flow rate of total gas (mL·min^{-1}); $CO_{2,\ in}$ and $CO_{2,\ out}$ are the molar concentration of CO_2 in the feed and product stream, respectively; Ar_{in} and Ar_{out} are the molar concentration of Ar in the feed and product stream respectively; $product_{out}$ is the molar concentration of products, and n is the number of carbon atoms in the product; $r_{RWGS,\ p}$ and $r_{CH_4,\ p}$ are the reaction rates of RWGS and CO_2 methanation, respectively; $S_{CH_4,\ p}$ and $S_{CO,\ p}$ stand for the selectivity to CH_4 and CO at zero of CO_2 conversion, respectively, and are obtained after an extrapolation of curves (CO and CH_4 selectivity versus CO_2 conversion) to zero of CO_2 conversion; *GHSV* represents gas hourly space velocity; $m_{CO_2,\ in}$ represents the molar fraction of CO_2 in the inlet gas; W_{Fe} represents the mass percentage of Fe in the catalyst; V_m represents molar volume at the standard temperature and pressure.

3. Result and discussion

3.1. Physical properties of fresh carbon-supported Fe-based catalysts

Fig. 4a shows that the combustion temperature of the catalysts, determined by TGA, decreases with increasing K loading, likely due to the promotion of defect formation on the carbon support surface by K. [64] The percentage of residual weight after complete combustion of the carbon support reflects the total Fe and K loading in the catalyst, while their molar ratios was determined using XRF analysis. The experimentally determined Fe loading and molar ratios of K: Fe are comparable with the theoretical values (Table 1).

From Fig. 4b, the H_2-TPR profiles show two predominant reduction peaks. The first peak, observed in the range of 250–400 °C, can be ascribed to the reduction of Fe_2O_3 to Fe_3O_4, while the second peak, appearing between 400 and 450 °C, corresponds to the subsequent reduction of Fe_3O_4 to metallic Fe. [65] Notably, the reduction peak associated with the Fe_2O_3 to Fe_3O_4 shifts toward higher temperatures with increasing K/Fe ratios, suggesting that the incorporation of K suppresses the reducibility of Fe_2O_3. This effect can be attributed to the strengthened Fe-O bond interactions in the presence of K. [66] In contrast, the peak corresponding to the reduction of Fe_3O_4 to metallic Fe shifts to lower temperatures (with the exception of K/Fe_0.5), indicating that K facilitates this reduction step. This promotion is likely related to the potassium agglomeration on the catalyst surface. [66]

Table 1 summarizes the elemental composition and physical properties of fresh carbon-supported Fe-based catalysts with various K/Fe molar ratios. For the catalysts with the K/Fe ratio ≤ 0.1, similar surface areas are observed. As the K/Fe ratio increased beyond this threshold, the surface area decreased by more than 20% as K loading doubled. No significant change in the pore volume and average pore diameter is found with increasing K/Fe ratio. All catalysts have typical IV N_2 adsorption-desorption isotherms, representing the presence of mesopores, as shown in Figure S8a. The XRD patterns (Figure S8b) reveal diffraction peaks corresponding to γ-Fe_2O_3 (PDF#39–1346), with the reflections at 2θ=30.2°, 35.6°, 43.3°, 57.3°, and 62.9°, attributed to (220), (311), (400), (511), and (440) planes, respectively. [67] TEM images (Fig. 5) present a uniform dispersion of Fe nanoparticles. The average Fe nanoparticle sizes obtained by TEM images were similar at around 9 nm among the fresh catalysts (Table 1), and their Fe nanoparticle size distributions were also comparable (Figure S9a), indicating that variation in the K/Fe ratio had minimal impact on the Fe nanoparticle size of fresh catalysts.

3.2. Effect of K on the CO_2 conversion

Fig. 6a shows the CO_2 conversion versus residence time over the carbon-supported Fe-based catalysts with various K/Fe ratios. As expected, CO_2 conversion has a positive relationship with residence time for all catalysts. At shorter residence times below 2 s, and with the CO_2 conversions below the RWGS equilibrium limit of 23%, the conversion trend follows K/Fe_0.1 > K/Fe_0.25 > K/Fe_0.5 > K/Fe_0.05 > K/Fe_0.02 > Bare Fe. Accordingly, CO_2 conversion increases with the K/Fe

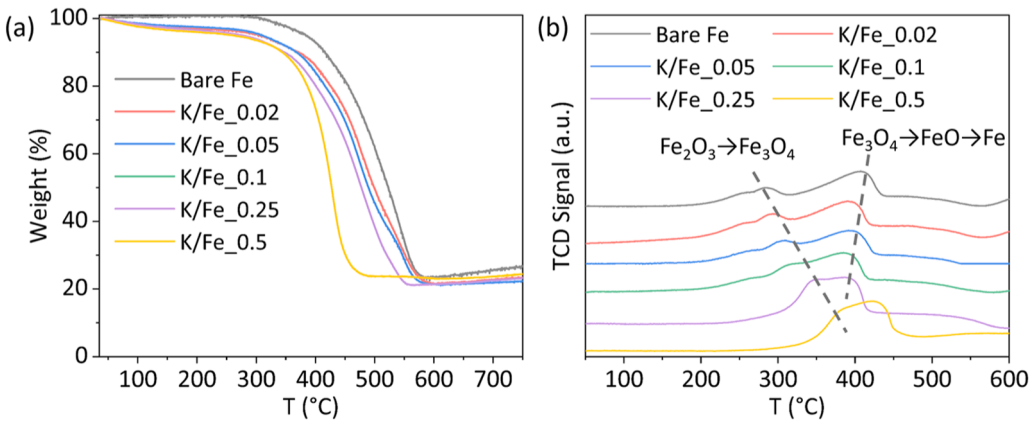

Fig. 4. (a) TGA curves and (b) H_2-TPR profiles of carbon-supported Fe-based catalysts with various K/Fe ratios.

Table 1
Physical properties of carbon-supported Fe-based catalysts with various K/Fe ratios.

Catalysts	Fe (wt%) [a,b]	K (wt%) [a,b]	K: Fe [b,c]	S_{BET} ($m^2 \cdot g^{-1}$) [d]	V_{SPD} ($cm^3 \cdot g^{-1}$) [d]	D_{BJH} (nm) [d]	$d_F \pm \sigma_F$ (nm) [e]	$d_S \pm \sigma_S$ (nm) [e,f]
Bare Fe	16	-	-	121	0.6	20	9.6±1.8	10.6±2.3
K/Fe_0.02	15	0.2	0.02	123	0.5	16	8.2±1.5	9.2±2.2
K/Fe_0.05	15	0.4	0.04	122	0.5	17	8.1±1.4	9.8±2.6
K/Fe_0.1	14	0.8	0.08	117	0.5	17	8.1±1.4	20.5±2.7
K/Fe_0.25	15	2	0.2	93	0.5	20	7.8±1.5	25.0±9.0
K/Fe_0.5	14	3.8	0.4	70	0.5	24	8.6±2.2	25.4±9.0

[a] measured by TGA;
[b] measured by XRF;
[c] molar ratio;
[d] measured by N_2 physisorption;
[e] measured by TEM;
[f] spent catalysts.

molar ratio till a maximum of K/Fe molar=0.1, as shown in Fig. 6b. Further increase in K/Fe ratios result in a decline in CO_2 conversion, although these catalysts still outperform the catalysts with lower K/Fe ratios. At longer residence times above 2 s, and with the CO_2 conversions above the RWGS equilibrium of 23%, the trend changes to K/Fe_0.1 > K/Fe_0.05 > K/Fe_0.02 ≥ Bare Fe > K/Fe_0.25 > K/Fe_0.5. The K/Fe_0.1 catalyst remains the most active, but in this region, catalysts with lower K/Fe ratios have comparable or even higher conversion than those with higher K/Fe ratios (Fig. 6b). This is different from the trend observed at shorter residence times and at lower CO_2 conversions. As established in our previous work, [60] RWGS dominates at CO_2 conversions below 23%, corresponding to the RWGS equilibrium conversion at 300 °C, 11 bar, H_2/CO_2=3 used in the study. At CO_2 conversion above 23%, FTS becomes the rate-determining process for overall CO_2 conversion. In this current study, the K/Fe ratio appears to exert distinct effects on the RWGS and FTS activities, despite both showing the same optimal K/Fe ratio.

3.3. Effect of K on the reaction pathway

The reaction pathway is elucidated by analyzing the relations between product selectivity and CO_2 conversion, as illustrated in Fig. 7. CO selectivity decreases with an increase in the CO_2 conversion (Fig. 7a), indicating that CO is directly formed from CO_2 via RWGS as the primary reaction and is subsequently consumed in downstream reactions. Extrapolating to zero CO_2 conversion, bare Fe, K/Fe_0.05, and K/Fe_0.02 catalysts show 91%, 95% and 97% CO selectivity, respectively, while the other catalysts show 100% CO selectivity. Correspondingly, the CH_4 selectivities for bare Fe, K/Fe_0.05, and K/Fe_0.02 catalysts are 9%, 5% and 3% respectively, when extrapolating to zero conversion (Fig. 7b), suggesting that CO_2 methanation occurs as a competing primary reaction on these catalysts. This competing reaction is progressively suppressed with increasing K/Fe ratio, and for catalysts with K/Fe ratios ≥ 0.1, RWGS dominates as the sole primary reaction and no CO_2 methanation occurs. The contribution of CO_2 methanation is estimated from the ratio of CH_4 selectivity to CO selectivity when extrapolating to CO_2 conversion, as summarized in Table 2. This ratio decreases from 0.1 for bare Fe to 0 and remains at 0 with further increases in the K/Fe ratio.

As CO_2 conversion increases, selectivity towards CO decreases with corresponding increases towards all hydrocarbons, revealing that CO produced via RWGS is further converted through FTS to form hydrocarbons (Fig. 7a to c). The distribution of C_{2+} hydrocarbons among C_2-C_4 paraffins, C_2-C_4 olefins, and C_{5+} hydrocarbons is provided in Fig. 7d to f. Increases in C_2-C_4 olefin and C_{5+} hydrocarbon selectivities begin at lower CO_2 conversions than those of C_2-C_4 paraffins suggests that C_2-C_4 olefins and C_{5+} hydrocarbons are secondary products formed from CO via FTS, while C_2-C_4 paraffins are tertiary products formed through subsequent hydrogenation of C_2-C_4 olefins.

Several notable effects of K addition on reaction pathways are evident. Firstly, for the carbon-supported bare Fe catalyst, CO selectivity decreases from 91% to 24% as CO_2 conversion increases from 1% to 38%, with the decrease in CO selectivity distributed more towards CH_4 than C_{2+} products. In contrast, K/Fe catalysts, with K/Fe ≥ 0.1, channel this decrease in CO selectivity predominantly towards C_{2+} hydrocarbons, while methane formation remains limited at less than 13%. Secondly, C_2-C_4 paraffin selectivity decreases with increasing K/Fe ratio and stabilizes when the K/Fe ratio reaches 0.1, whereas C_2-C_4 olefins increase initially and then plateau. Consequently, the olefin to paraffin ratio of C_2-C_4 hydrocarbons rises at first and then becomes relatively constant with further K addition (Figure S10). These results can be attributed to the ability of K to suppress olefin hydrogenation by

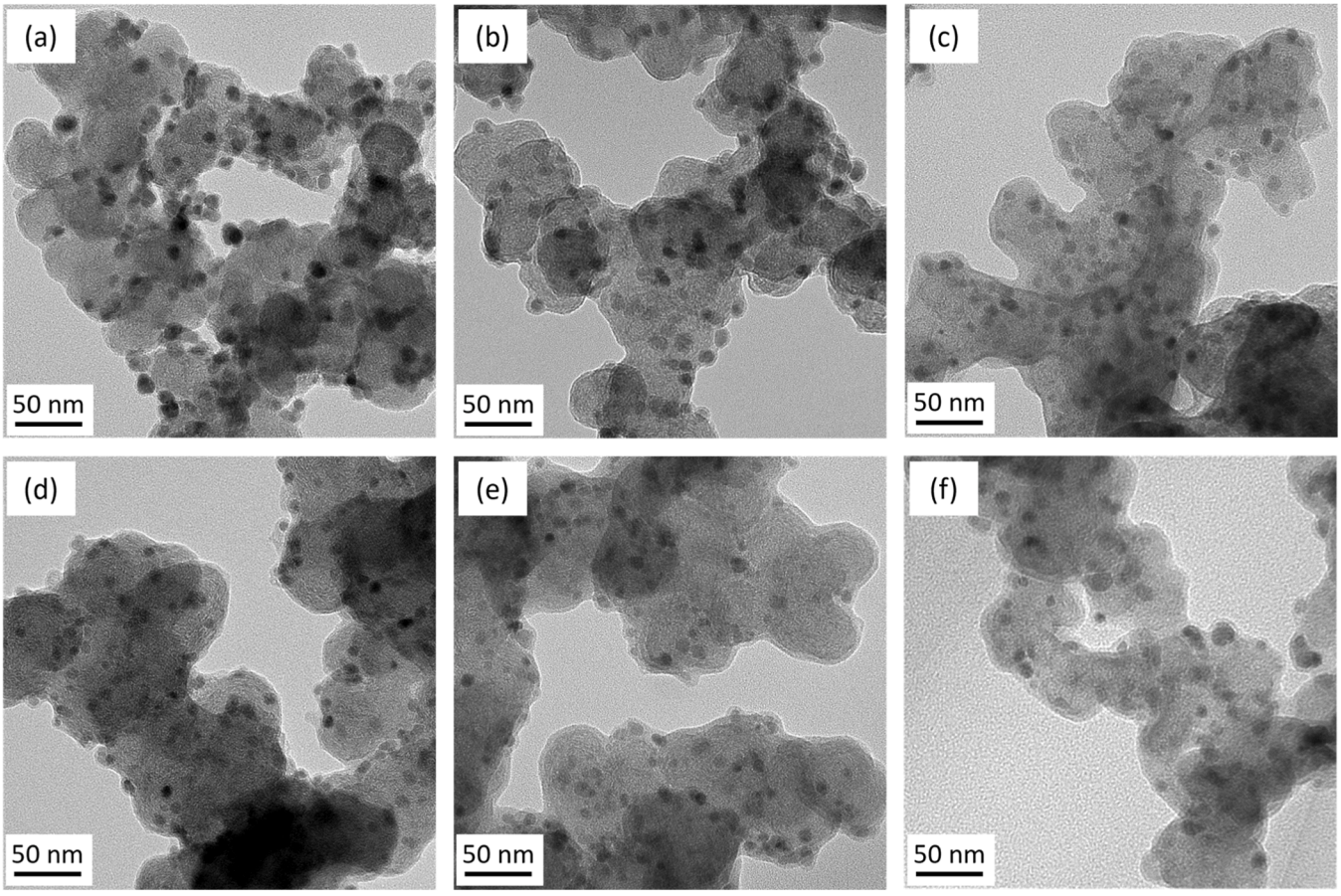

Fig. 5. TEM images of fresh carbon-supported Fe-based catalysts: (a) bare Fe, (b) K/Fe_0.02, (c) K/Fe_0.05, (d) K/Fe_0.1, (e) K/Fe_0.25, and (f) K/Fe_0.5.

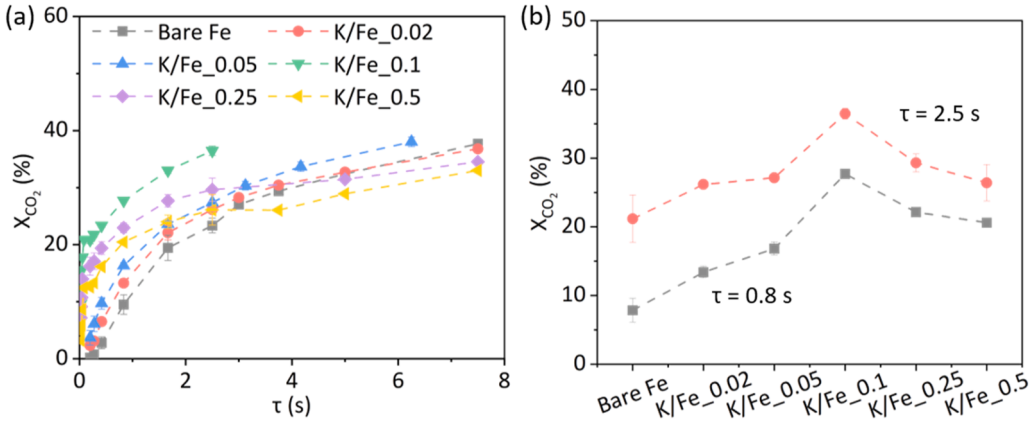

Fig. 6. CO_2 conversion versus residence time over the carbon-supported Fe-based catalysts with various K/Fe ratios.

inhibiting H_2 adsorption. [68–70] Thirdly, C_{5+} selectivity first increases with the K/Fe ratio, attains a maximum at a moderate K/Fe ratio, and declines at a higher ratio. This demonstrates that an optimal K/Fe ratio facilitates C-C coupling, while excessive K hinders the formation of C_{5+} hydrocarbons, which can be owing to the decreased reduction degree, specific surface area, and graphitization degree of the catalysts. [64]

3.4. Effect of K on RWGS

The RWGS equilibrium conversion at the conditions employed in this study (300 °C, 11 bar, H_2/CO_2=3) is 23%. RWGS predominates at CO_2 conversion below this threshold while FTS becomes more significant with increasing conversion. Notably, CO selectivity remains above 80% for all catalysts below 15% CO_2 conversion, indicating the dominance of RWGS in this regime. Accordingly, the effect of K on the RWGS reaction is evaluated at CO_2 conversion below 15% to minimize the influence of FTS. Section 3.2 and 3.3 address the effect of K on RWGS activity and reaction pathway; here, the focus is on selectivity. To further clarify the effect of the K/Fe ratio on the selectivity of RWGS, the catalytic performance at 7% CO_2 conversion is compared in Fig. 8a. The carbon-supported bare Fe catalyst shows the lowest CO selectivity of 88%, accompanied by the highest CH_4 selectivity of 10%, revealing a strong tendency toward methanation. Upon the introduction of K, CO selectivity increases, reaching 97% for the K/Fe_0.5 catalyst, while CH_4

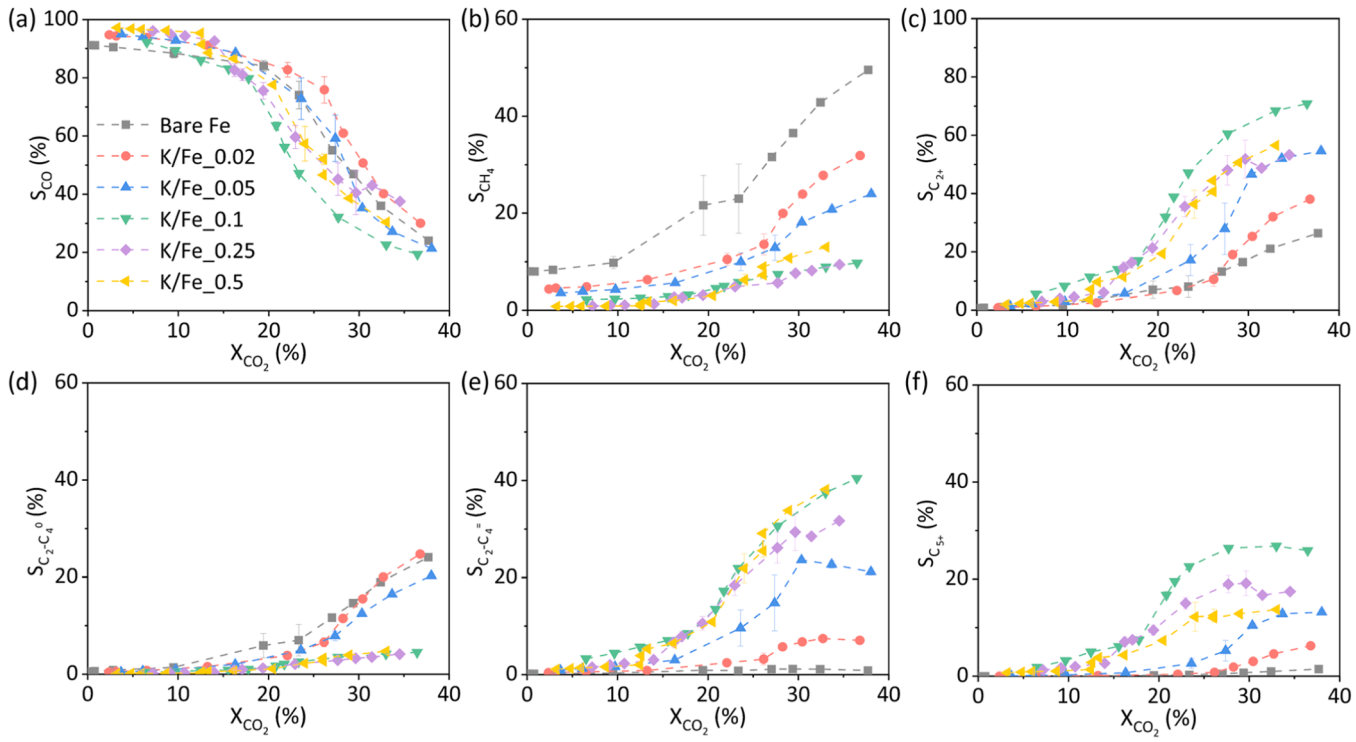

Fig. 7. Product selectivity-conversion relationships for (a) CO, (b) CH_4, (c) C_{2+}, (d) C_2-C_4^0, (e) C_2-$C_4^=$, and (f) C_{5+} over the carbon-supported Fe-based catalysts with various K/Fe ratios.

Table 2
The rate ratio of primary reactions (RWGS and CO_2 methanation) at zero CO_2 conversion.

Catalysts	$S_{CH_4,\ p}$(%)	$S_{CO,\ p}$(%)	$\frac{r_{CH_4,\ p}}{r_{RWGS,\ p}}$
Bare Fe	9	91	0.1
K/Fe_0.02	5	95	0.05
K/Fe_0.05	3	97	0.03
K/Fe_0.1	0	100	0
K/Fe_0.25	0	100	0
K/Fe_0.5	0	100	0

selectivity decreases correspondingly. These results imply that a higher K/Fe ratio promotes a more selective RWGS process and suppresses excessive hydrogenation, leading to improved CO selectivity. Besides, the formation rates of the products were shown in Fig. 8b. The formation rate of CO is significantly higher than that of hydrocarbon formation. The CO formation rate initially increases with the K/Fe ratio, reaches a maximum at K/Fe = 0.1, and then decreases with further K addition.

Quasi in situ Mössbauer spectroscopy was performed to identify the Fe phases, and detailed fitting parameters are provided in Figure S11, Tables S3, S4 and S5. The Fe phase distributions of fresh, reduced, and carburized catalysts are shown in Figure S12. All fresh catalysts consist entirely of Fe_2O_3. After reduction, the catalysts contain similar amounts of Fe^0 (23–28%) and FeO (62–67%), indicating that the K/Fe ratio does not significantly affect catalyst reducibility. This behavior could be attributed to sufficient time for the reduction process to reach completion. After carburization, the carbon-supported bare Fe catalyst consists of 39% ε'-$Fe_{2.2}C$ and 61% FeO whereas both K/Fe catalysts are fully carburised, containing at least twice as much ε'-$Fe_{2.2}C$ as χ-Fe_5C_2. Notably, the content of χ-Fe_5C_2 increases with the increasing K/Fe ratio upon carburisation.

For the catalysts measured quasi in situ after the RWGS reaction conditions as presented in Fig. 8c, the carbon-supported bare Fe catalyst

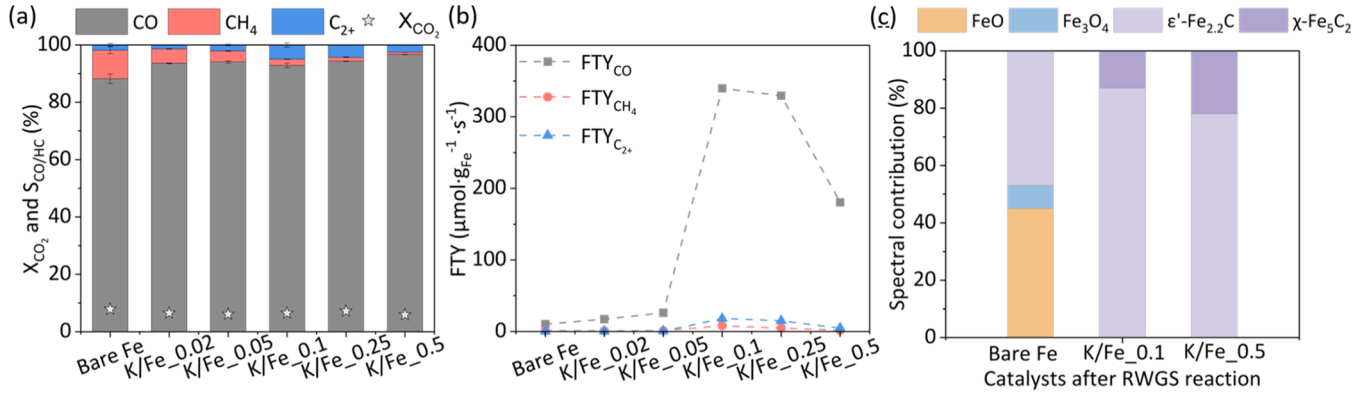

Fig. 8. (a) Catalytic performance and (b) FTY of products for RWGS at $X_{CO2} \approx 7\%$, and (c) distribution of Fe phase after RWGS reaction at lower CO_2 conversion over the carbon-supported Fe-based catalysts with various K/Fe ratios.

consists of 45% FeO, 8% Fe_3O_4, and 47% ε'-$Fe_{2.2}C$. On the other hand, the K/Fe_0.1 catalyst contains 87% ε'-$Fe_{2.2}C$ and 13% χ-Fe_5C_2, while K/Fe_0.5 contains 78% ε'-$Fe_{2.2}C$ and 22% χ-Fe_5C_2. Comparing the carbide composition in K/Fe_0.1 and K/Fe_0.5 after carburisation and RWGS, the ε'-$Fe_{2.2}C$ phase increases by 8 ± 2% while the χ-Fe_5C_2 phase show a corresponding decrease. Nonetheless, the carbide phases remain stable upon carburisation and RWGS, and we hypothesize that the carbon support and K promotion contribute to stabilizing these carbides. Importantly, K/Fe_0.1 and K/Fe_0.5 catalysts consist exclusively of ε'-$Fe_{2.2}C$ and χ-Fe_5C_2, yet they are highly active and selective towards RWGS, indicating that the Fe carbides are responsible for RWGS.

3.5. Effect of K on FTS

The effect of K on FTS is discussed at comparable CO_2 conversion of approximately 33%, as shown in Fig. 9a. The influence of K promoter on CO selectivity under FTS conditions differs from that observed under RWGS conditions: the K/Fe_0.02 catalyst displays the highest CO selectivity, while the K/Fe_0.1 catalyst shows the lowest. The variation in CO selectivity could depend on the competing CO_2 methanation and the secondary FTS reaction. CH_4 selectivity generally decreases with increasing K/Fe ratio, although a slight increase is observed at the highest K/Fe ratio, indicating that K suppresses methanation. The C_{2+} selectivity follows the order: K/Fe_0.1 > K/Fe_0.25 ≥ K/Fe_0.5 > K/Fe_0.05 > K/Fe_0.02 > Bare Fe, suggesting that a moderate K/Fe ratio of 0.1 provides the optimal balance for promoting higher hydrocarbon formation in FTS. As shown in Fig. 9b, the formation rate of CH_4 decreases continuously as the K/Fe ratio increases. In contrast, the formation rate of C_{2+} hydrocarbon first increases and reaches its highest value at K/Fe=0.1, followed by a decline at higher K/Fe ratios.

Fig. 9c shows the Fe phases after the FTS reaction conditions. The carbon-supported bare Fe catalyst consists of 56% Fe_3O_4 and 44% ε'-$Fe_{2.2}C$. Compared to the Fe phase after the RWGS reaction conditions, bare Fe shows a lack of FeO, a higher proportion of Fe_3O_4 and a lower fraction of ε'-$Fe_{2.2}C$, indicating partial oxidation occurred after the FTS reaction. The increased CO_2 conversion resulting in higher H_2O formation may account for this oxidation. K/Fe_0.1 contains 77% ε'-$Fe_{2.2}C$ and 23% χ-Fe_5C_2, and K/Fe_0.5 catalyst contains 80% ε'-$Fe_{2.2}C$ and 20% χ-Fe_5C_2. These results suggest that the Fe carbides are the active phases in the FTS reaction. It is worth noting that ε'-$Fe_{2.2}C$ and χ-Fe_5C_2 may have different catalytic ability, with χ-Fe_5C_2 possibly promoting the formation of long-chain hydrocarbons. For the K-promoted catalysts, the formation of χ-Fe_5C_2 increases for K/Fe_0.1, but decreases for K/Fe_0.5 under FTS reaction conditions. This suggests that an optimal K/Fe ratio is beneficial for the formation and stabilization of χ-Fe_5C_2 during the FTS reaction.

3.6. Effect of K on the particle size growth after reaction

Fig. 10 displays the TEM images of the spent carbon-supported Fe-based catalysts with various K/Fe ratios after 37 h on stream, and corresponding average nanoparticle sizes are summarized in Table 1. As the K/Fe ratio increases, a clear growth in the average Fe nanoparticle size after reaction is observed. For the catalysts without or with K/Fe ratios lower than 0.1, the nanoparticles have a relatively narrow size distribution (Figure S9b), and the growth in average nanoparticle size is limited to less than 20%. For catalysts with higher K/Fe ratios, the particle size distribution becomes significantly broader (Figure S9b), and the average particle size increases by more than 100%. These results clearly demonstrate that increasing the K/Fe ratio results in severe sintering, which is consistent with previous reports. [28]

4. Conclusion

A series of carbon-supported Fe-based catalysts with various K/Fe molar ratios from 0.02 to 0.5 was prepared to investigate the effect of K on reaction pathways in the direct CO_2 hydrogenation to higher hydrocarbons. All fresh catalysts consist of Fe_2O_3 nanoparticles with an average size of 9 nm, indicating that K addition had no influence on catalyst synthesis. The addition of K did not influence catalyst reduction, yet resulted in complete carburization after the carburization procedure. Catalytic performance was carried out at 300 °C, 11 bar, $H_2/CO_2/Ar$=3/1/1, 1000–375000 mL·g_{cat}^{-1}·h^{-1}. Increasing the K/Fe ratio progressively adjusted the reaction mechanism by suppressing primary CO_2 methanation, which competes with the RWGS primary reaction, until it eventually disappeared, while FTS remained as the secondary reaction. As RWGS and FTS are primary and secondary reaction pathways, the influence of K on RWGS was evaluated at a CO_2 conversion of ~7%, and its effect on FTS was assessed at ~33% CO_2 conversion. Increasing the K/Fe ratio from 0.02 to 0.5 promoted the RWGS reaction relative to the competing CO_2 methanation, resulting in the highest CO selectivity reported for the K/Fe_0.5 catalyst. On the other hand, the K/Fe_0.1 catalyst showed the highest selectivity towards C_{2+} hydrocarbons. Quasi in situ Mössbauer spectroscopy revealed that after RWGS and FTS conditions, both K/Fe_0.1 and K/Fe_0.5 consisted of around 80% ε'-$Fe_{2.2}C$ and 20% χ-Fe_5C_2. The resulting Fe carbides remained stable after both RWGS and FTS conditions, likely due to the carbon support and K promotion, suggesting that they are responsible for catalyzing both reactions. This finding contrasts with literature reports that attribute RWGS and FTS activity to Fe oxides and Fe carbides, respectively. In addition, increasing the K/Fe ratio results in severe sintering. Overall, there is an optimal K/Fe ratio (K/Fe_0.1) on RWGS and FTS activity. In terms of selectivity, a higher K/Fe ratio is beneficial to the CO selectivity of RWGS, and K/Fe_0.1 remains the most active for the long-chain

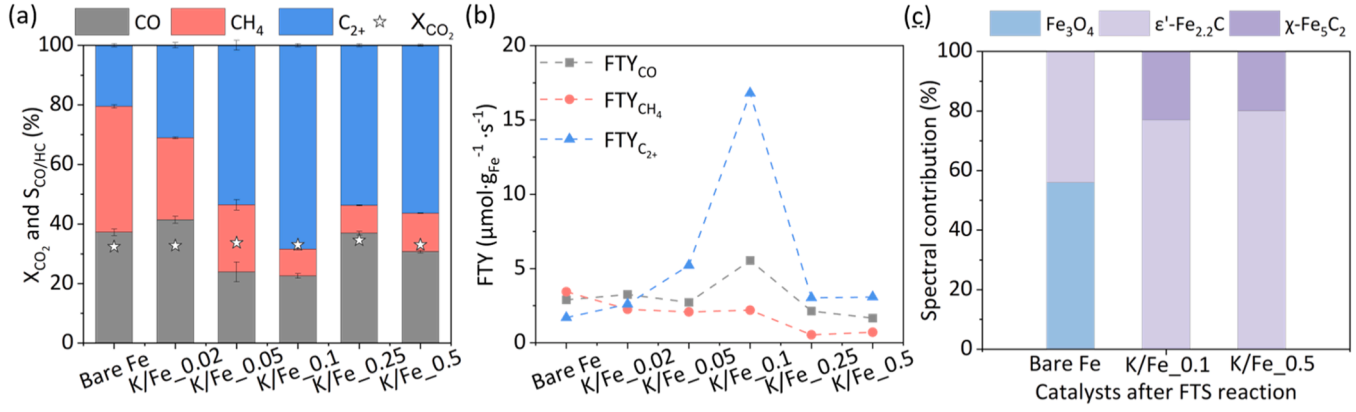

Fig. 9. (a) Catalytic performance and (b) FTY of products for FTS at X_{CO2} ≈ 33%, and (c) distribution of Fe phase after FTS reaction at higher CO_2 conversion over the carbon-supported Fe-based catalysts with various K/Fe ratios.

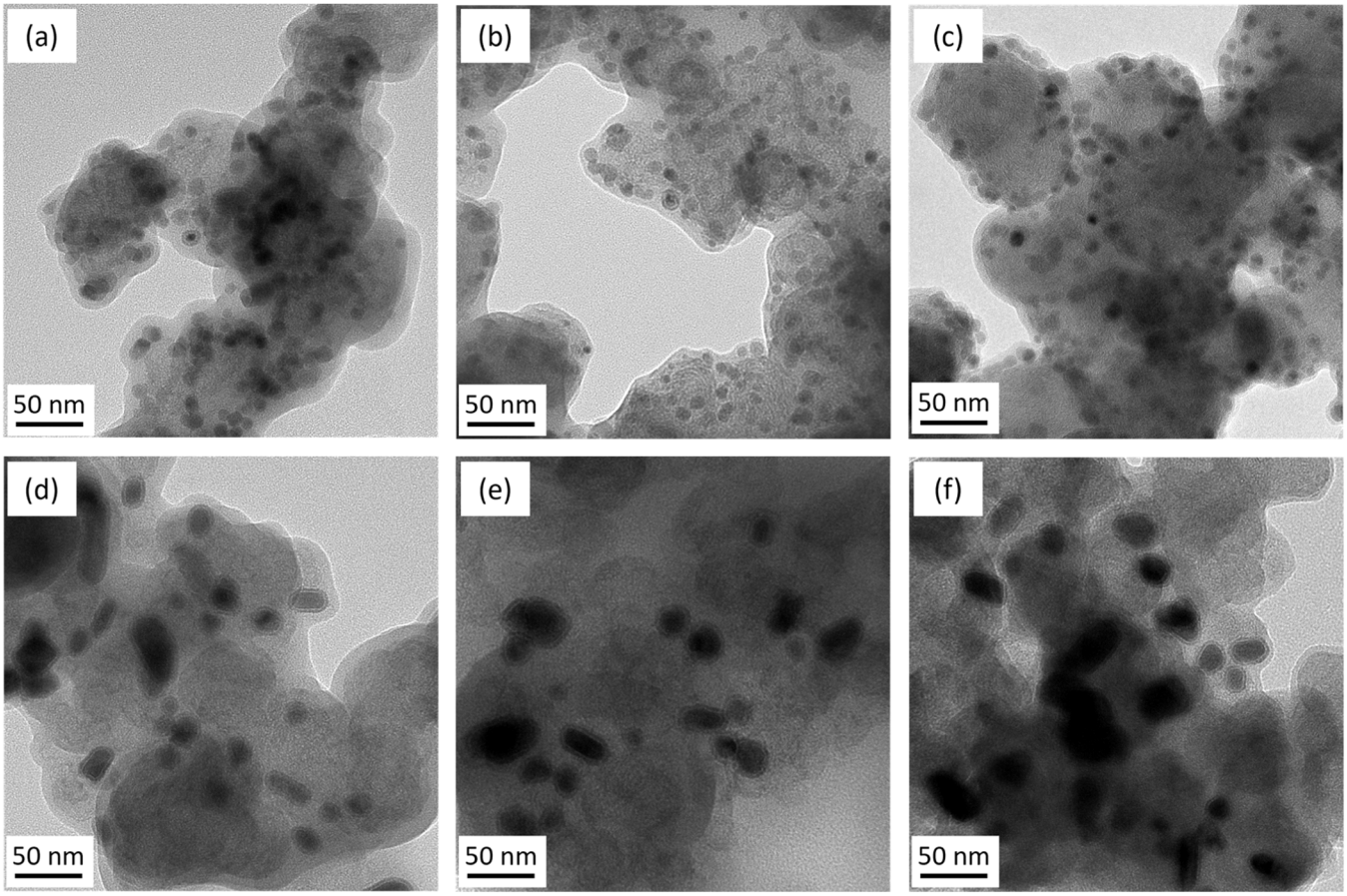

Fig. 10. TEM images of spent carbon-supported Fe-based catalysts: (a) bare Fe, (b) K/Fe_0.02, (c) K/Fe_0.05, (d) K/Fe_0.1, (e) K/Fe_0.25, and (f) K/Fe_0.5 (TOS=37 h, 300 °C, 11 bar, GHSV=3000–37500 mL·g_{cat}^{-1}·h^{-1}).

hydrocarbons.

CRediT authorship contribution statement

Jingxiu Xie: Writing – review & editing, Writing – original draft, Supervision, Resources, Project administration, Methodology, Funding acquisition, Formal analysis, Conceptualization. **Renske Rocks:** Writing – review & editing, Methodology, Investigation, Data curation, Conceptualization. **A. Iulian Dugulan:** Writing – review & editing, Validation, Resources, Methodology, Investigation, Formal analysis, Data curation, Conceptualization. **Weixin Meng:** Writing – review & editing, Writing – original draft, Validation, Methodology, Investigation, Formal analysis, Data curation, Conceptualization.

Declaration of Competing Interest

The authors declare that they have no known competing financial interests or personal relationships that could have appeared to influence the work reported in this paper.

Acknowledgment

Weixin Meng acknowledges financial support from the China Scholarship Council (CSC): NO. 202106460008. Dr. Leendert Bezemer from Shell is acknowledged for scientific discussions.

Appendix A. Supporting information

Supplementary data associated with this article can be found in the online version at doi:10.1016/j.jcou.2026.103543.

Data Availability

Data will be made available on request.

References

[1] Q.A. Nwabueze, S. Leggett, Advancements in the application of CO_2 capture and utilization technologies - a comprehensive review, Fuels 5 (3) (2024) 508–532, https://doi.org/10.3390/fuels5030028.
[2] R. Estevez, L. Aguado-Deblas, F.M. Bautista, F.J. López-Tenllado, A.A. Romero, D. Luna, A review on green hydrogen valorization by heterogeneous catalytic hydrogenation of captured CO_2 into value-added products, Catal 12 (12) (2022) 1555, https://doi.org/10.3390/catal12121555.
[3] M.I.; Alam, R.; Cheula, G.; Moroni, L.; Nardi, M. Maestri, Mechanistic and multiscale aspects of thermo-catalytic CO_2 conversion to C_1 products, Catal. Sci. Technol. 11 (2021) 6601–6629, https://doi.org/10.1039/D1CY00922B.
[4] X.; Lu, K.; Tan, J.; Zhao, G. Zhan, Advances in integrated catalysts for CO_2 thermal hydrogenation to multicarbon products, Chem. Catal. 5 (3) (2025) 101264, https://doi.org/10.1016/j.checat.2025.101264.
[5] J.; Wei, R.; Yao, Y.; Han, Q.; Ge, J. Sun, Towards the development of the emerging process of CO_2 heterogenous hydrogenation into high-value unsaturated heavy hydrocarbons, Chem. Soc. Rev. 50 (2021) 10764–10805, https://doi.org/10.1039/D1CS00260K.
[6] F.; Lu, B.; Sun, J.; Feng, J.; Jiang, W. Xu, Recent progress for boosting CO_2 hydrogenation to light olefins, Appl. Catal. A Gen. 687 (2024) 119982, https://doi.org/10.1016/j.apcata.2024.119982.
[7] Y.; Shi, W.; Gao, G.; Liu, N. Tsubaki, A review of CO_2 hydrogenation to liquid fuels, ChemSusChem (2025) e202402756, https://doi.org/10.1002/cssc.202402756.
[8] R.; Ye, J.; Ding, T.R.; Reina, M.S.; Duyar, H.; Li, W.; Luo, R.; Zhang, M.; Fan, G.; Feng, J.; Sun, J. Liu, Design of catalysts for selective CO_2 hydrogenation, Nat. Synth. 4 (2025) 288–302, https://doi.org/10.1038/s44160-025-00747-1.
[9] S.; Najari, S.; Saeidi, A.; Sápi, Á.; Szamosvölgyi, Á.; Papp, A.; Efremova, H.; Bali, Z. Kónya, Synergistic enhancement of CO_2 hydrogenation to C_{5+} hydrocarbons using mixed Fe_5C_2 and Na-Fe_3O_4 catalysts: Effects of oxide/carbide ratio, proximity, and reduction, CEJ 485 (2024) 149787, https://doi.org/10.1016/j.cej.2024.149787.

[10] L.; Tang, B.; Zhou, X.; Liu, S.; Xu, J.; Wang, W.; Xu, X.; Liu, L.; Chen, A. Lu, Selective synthesis of the core-shell structured catalyst χ-Fe_5C_2 surrounded by nanosized Fe_3O_4 for the conversion of syngas to liquid fuels, Catal. Sci. Technol. 12 (2022) 1978, https://doi.org/10.1039/d1cy02241e.

[11] D.; Ye, W.; Tang, T.; Zhang, L.; Lv, Z.; Zou, R.K.; Gupta, S. Tang, Enhancing the synergism of Fe_3O_4 and Fe_5C_2 to improve the process of CO_2 hydrogenation to olefines, Colloids Surf. A 654 (2022) 130145, https://doi.org/10.1016/j.colsurfa.2022.130145.

[12] J.; Tafjord, S.K. Regli, A.I.; Dugulan, M.; Rønning, E.; Rytter, A.; Holmen, R.; Myrstad, J. Yang, Influence of temperature during pyrolysis of Fe-alginate: Unraveling the pathway towards highly active Fe/C catalysts, Appl. Catal. A Gen. 644 (2022) 118834, https://doi.org/10.1016/j.apcata.2022.118834.

[13] R.; Yao, J.; Wei, Q.; Ge, J.; Xu, Y.; Han, H.; Xu, J. Sun, Structure sensitivity of iron oxide catalyst for CO_2 hydrogenation, Catal. Today 371 (2021) 134–141, https://doi.org/10.1016/j.cattod.2020.07.073.

[14] Y.; Chen, K. Huo, Y.; Wang, Q. Li, D.; Li, Z.; Yuan, Y.; Liu, X.; Gao, Y.; Lu, T.; Xing, J.; Sui, Q.; Liu, W.; Wang, G.; Yang, N.; Tsubaki, M. Wu, The impact of initial particle size on the dynamic structure evolution of Fe-based active site in CO_2 hydrogenation and the structure-function relationship for C_{2+} products synthesis, J. Catal. 456 (2026) 116788, https://doi.org/10.1016/j.jcat.2026.116788.

[15] J.; Kirchner, Z.; Baysal, S. Kureti, Activity and structural changes of Fe-based catalysts during CO_2 hydrogenation towards CH_4 - A mini review, ChemCatChem 12 (2020) 981, https://doi.org/10.1002/cctc.201901956.

[16] Q.; Yang, A.; Skrypnik, A.; Matvienko, H.; Lund, M.; Holena, E.V. Kondratenko, Revealing property-performance relationships for efficient CO_2 hydrogenation to higher hydrocarbons over Fe-based catalysts: Statistical analysis of literature data and its experimental validation, Appl. Catal. B Environ. 282 (2021) 119554, https://doi.org/10.1016/j.apcatb.2020.119554.

[17] B.; Liang, H.; Duan, T.; Sun, J.; Ma, X.; Liu, J.; Xu, X.; Su, Y.; Huang, T. Zhang, Effect of Na promoter on Fe-based catalyst for CO_2 hydrogenation to alkenes, ACS Sustain. Chem. Eng. 7 (2019) 925–932, https://doi.org/10.1021/acssuschemeng.8b04538.

[18] X.; Ai, Y.; Zhang, Y.; Zhao, J.; Hong, C.; Liu, J. Li, $MnCO_3$ enhances Na-modified Fe_5C_2 catalyst for CO_2 hydrogenation to light olefins, Fuel 384 (2025) 133958, https://doi.org/10.1016/j.fuel.2024.133958.

[19] W. Yoon, H.; Jo, S.; Ahmed, M.K.; Khan, M.; Irshad, J.; Lee, S.S.; Bibi, J. Kim, Role of alkali metal in maintaining iron integrity during direct CO_2 hydrogenation, CEJ 495 (2024) 153617, https://doi.org/10.1016/j.cej.2024.153617.

[20] H. Yang, Y. Dang, X. Cui, X. Bu, J. Li, S. Li, Y. Sun, P. Gao, Selective synthesis of olefins via CO_2 hydrogenation over transition-metal-doped iron-based catalysts, Appl. Catal. B Environ. 321 (2023) 122050, https://doi.org/10.1016/j.apcatb.2022.122050.

[21] Q. Yang, H. Lund, S. Bartling, F. Krumeich, A.S. Skrypnik, E.V. Kondratenko, The role of Na for efficient CO_2 hydrogenation to higher hydrocarbons over Fe-based catalysts under externally forced dynamic conditions, J. Catal. 426 (2023) 126–139, https://doi.org/10.1016/j.jcat.2023.07.012.

[22] R.; Liu, Z.; Ma, J.D. Sears, M.; Juneau, M.L. Neidig, M.D. Porosoff, Identifying correlations in Fischer-Tropsch synthesis and CO_2 hydrogenation over Fe-based ZSM-5 catalysts, J. CO_2 Util. 41 (2020) 101290, https://doi.org/10.1016/j.jcou.2020.101290.

[23] B.; Rolandi, M.; Piacentini, R.; Ometto, A.; Porta, C.G. Visconti, On the performances of highly promoted Fe-Zn-Cu-K catalysts for CO_2 Fischer-Tropsch synthesis, Appl. Catal. A Gen. 708 (2025) 120590, https://doi.org/10.1016/j.apcata.2025.120590.

[24] L. Guo, J. Sun, X. Ji, J.; Wei, Z.; Wen, R.; Yao, H.; Xu, Q. Ge, Directly converting carbon dioxide to linear α-olefins on bio-promoted catalysts, Commun. Chem. 1 (2018) 11, https://doi.org/10.1038/s42004-018-0012-4.

[25] Y.; Han, C.; Fang, X.; Ji, J.; Wei, Q.; Ge, J. Sun, Interfacing with carbonaceous potassium promoters boosts catalytic CO_2 hydrogenation of iron, ACS Catal. 10 (20) (2020) 12098–12108, https://doi.org/10.1021/acscatal.0c03215.

[26] C.G.; Visconti, M.; Martinelli, L.; Falbo, A.; Infantes-Molina, L.; Lietti, P.; Forzatti, G.; Iaquaniello, E.; Palo, B.; Picutti, F. Brignoli, CO_2 hydrogenation to lower olefins on a high surface area K-promoted bulk Fe-catalyst, Appl. Catal. B Environ. 200 (2017) 530–542, https://doi.org/10.1016/j.apcatb.2016.07.047.

[27] Q.; Yang, V.A. Kondratenko, S.A. Petrov, D.E. Doronkin, E.; Saraçi, H.; Lund, A.; Arinchtein, R.; Kraehnert, A.S. Skrypnik, A.A. Matvienko, E.V. Kondratenko, Identifying performance descriptors in CO_2 hydrogenation over iron-based catalysts promoted with alkali metals, Angew. Chem. Int. Ed. 61 (2022) e202116517, https://doi.org/10.1002/anie.202116517.

[28] H.; Chang, Q.; Lin, M.; Cheng, K.; Zhang, B.; Feng, J.; Chai, Y.; Lv, Z. Men, Effects of potassium loading over iron-silica interaction, phase evolution and catalytic behavior of precipitated iron-based catalysts for Fischer-Tropsch synthesis, Catal 12 (2022) 916, https://doi.org/10.3390/catal12080916.

[29] Y.; Yu, A.; Asokan, M.E. Suss, A. Yu, D.S.A. Simakov, Reverse microemulsion synthesis promotes the formation of iron carbide in direct hydrogenation of CO_2 to light hydrocarbons, Catal. Today 441 (2024) 114896, https://doi.org/10.1016/j.cattod.2024.114896.

[30] N. Fischer, R. Henkel, B. Hettel, M. Iglesias, G. Schaub, M. Claeys, Hydrocarbons via CO_2 hydrogenation over iron catalysts: The effect of potassium on structure and performance, Catal. Lett. 146 (2016) 509–517, https://doi.org/10.1007/s10562-015-1670-9.

[31] Y.; Yang, H.; Zhang, H.; Ma, W.; Qian, Q.; Sun, W. Ying, Effect of alkalis (Li, Na, and K) on precipitated iron-based catalysts for high-temperature Fischer-Tropsch synthesis, Fuel 326 (2022) 125090, https://doi.org/10.1016/j.fuel.2022.125090.

[32] X.; Nie, L.; Meng, H.; Wang, Y.; Chen, X.; Guo, C. Song, DFT insight into the effect of potassium on the adsorption, activation and dissociation of CO_2 over Fe-based catalysts, Phys. Chem. Chem. Phys. 20 (2018) 14694, https://doi.org/10.1039/c8cp02218f.

[33] X.; Ren, R.D.E. Krösschell, Z.; Men, P.; Wang, I.A.W. Filot, E.J.M. Hensen, A theoretical study of the role of K on the reverse water-gas shift reaction on Hägg carbide, Chin. J. Catal. 72 (2025) 289–300, https://doi.org/10.1016/S1872-2067(24)60278-0.

[34] H.; Tang, T.; Qiu, X.; Wang, C.; Zhang, Z. Zhang, A brief review of recent theoretical advances in Fe-based catalysts for CO_2 hydrogenation, Molecules 29 (2024) 1194, https://doi.org/10.3390/molecules29061194.

[35] Y.; Zhou, A.S.; Traore, D.V. Peron, A.J. Barrios, S.A. Chernyak, M.; Corda, O. V. Safonova, A.I.; Dugulan, O.; Ersen, M.; Virginie, V.V. Ordomsky, A.Y. Khodakov, Promotion effects of alkali metals on iron molybdate catalysts for CO_2 catalytic hydrogenation, J. Energy Chem. 85 (2023) 291–300, https://doi.org/10.1016/j.jechem.2023.06.019.

[36] J.; Zhu, S.; Shaikhutdinov, B.R. Cuenya, Structure-reactivity relationships in CO_2 hydrogenation to C_{2+} chemicals on Fe-based catalysts, Chem. Sci. 16 (2025) 1071–1092, https://doi.org/10.1039/D4SC06376G.

[37] Y.; Zhao, J.; Ma, J.; Yin, H. Han, X.; Zhang, Y.; Cao, W. Cai, Alkali metal promotion on Fe-Co-Ni trimetallic catalysts for CO_2 hydrogenation to light olefins, Appl. Surf. Sci. 657 (2024) 159783, https://doi.org/10.1016/j.apsusc.2024.159783.

[38] A.S. Skrypnik, S.A. Petrov, V.A. Kondratenko, Q.; Yang, A.A. Matvienko, E. V. Kondratenko, Spatially resolved analysis of CO_2 hydrogenation to higher hydrocarbons over alkali-metal promoted well-defined $Fe_xO_yC_z$, J. Catal. 425 (2023) 286–295, https://doi.org/10.1016/j.jcat.2023.06.019.

[39] J.A. Loiland, M.J. Wulfers, N.S. Marinkovic, R.F. Lobo, Fe/γ-Al_2O_3 and Fe-K/γ-Al_2O_3 as reverse water-gas shift catalysts, Catal. Sci. Technol. 6 (2016) 5267, https://doi.org/10.1039/c5cy02111a.

[40] P.; Tian, M.; Gu, R.; Qiu, Z.; Yang, F.; Xuan, M. Zhu, Tunable carbon dioxide activation pathway over iron oxide catalysts: Effects of potassium, Ind. Eng. Chem. Res. 60 (24) (2021) 8705–8713, https://doi.org/10.1021/acs.iecr.1c01592.

[41] W.; Zhang, J.; Sun, H.; Wang, X. Cui, Recent advances in hydrogenation of CO_2 to CO with heterogeneous catalysts through the RWGS reaction, Asian J. 19 (2024) e202300971, https://doi.org/10.1002/asia.202300971.

[42] M.; Amoyal, R.; Vidruk-Nehemya, M.V. Landau, M. Herskowitz, Effect of potassium on the active phases of Fe catalysts for carbon dioxide conversion to liquid fuels through hydrogenation, J. Catal. 348 (2017) 29–39, https://doi.org/10.1016/j.jcat.2017.01.020.

[43] N.; Utsis, M.V. Landau, A. Erenburg, R.V.; Nehemya, M. Herskowitz, Performance of reverse water gas shift on coprecipitated and C-Templated BaFe-Hexaaluminate: The effect of Fe loading, texture, and promotion with K, ChemCatChem 10 (2018) 3795–3805, https://doi.org/10.1002/cctc.201800709.

[44] D.M.; del Monte, A.J. Vizcaíno, J. Dufour, C. Martos, Effect of K, Co and Mo addition in Fe-based catalysts for aviation biofuels production by Fischer-Tropsch synthesis, Fuel Process. Technol. 194 (2019) 106102, https://doi.org/10.1016/j.fuproc.2019.05.025.

[45] X.; Ren, Z. Men, P.; Wang, I.A.W. Filot, E.J.M. Hensen, The nature of K promotion of χ-Fe_5C_2 for high chain-growth probability in the Fischer-Tropsch reaction, Appl. Catal. B Environ. Energy 374 (2025) 125403, https://doi.org/10.1016/j.apcatb.2025.125403.

[46] D.B. Bukur, D.; Mukesh, S.A. Patel, Promoter effects on precipitated iron catalysts for Fischer-Tropsch synthesis, Ind. Eng. Chem. Res. 29 (1990) 194–204.

[47] W.; Ma, E.L. Kugler, D.B. Dadyburjor, Potassium effects on activated-carbon-supported iron catalysts for Fischer-Tropsch synthesis, Energy & Fuels 21 (2007) 1832–1842, https://doi.org/10.1021/ef060654e.

[48] M.C. Ribeiro, G.; Jacobs, B.H. Davis, D.C. Cronauer, A.J.; Kropf, C.L. Marshall, Fischer-Tropsch synthesis: An in-situ TPR-EXAFS/XANES investigation of the influence of group I alkali promoters on the local atomic and electronic structure of carburized iron/silica catalysts, J. Phys. Chem. C. 114 (17) (2010) 7895–7903, https://doi.org/10.1021/jp911856q.

[49] H. Wan, B.; Wu, C.; Zhang, H.; Xiang, Y. Li, Promotional effects of Cu and K on precipitated iron-based catalysts for Fischer-Tropsch synthesis, J. Mol. Catal. A Chem. 283 (2008) 33–42, https://doi.org/10.1016/j.molcata.2007.12.013.

[50] A.P. Raje, R.J. O'Brien, B.H. Davis, Effect of potassium promotion on iron-based catalysts for Fischer-Tropsch synthesis, J. Catal. 180 (1998) 36–43, https://doi.org/10.1006/jcat.1998.2259.

[51] Y.; Yang, H.; Xiang, Y.; Xu, L.; Bai, Y. Li, Effect of potassium promoter on precipitated iron-manganese catalyst for Fischer-Tropsch synthesis, Appl. Catal. A Gen. 266 (2004) 181–194, https://doi.org/10.1016/j.apcata.2004.02.018.

[52] Z.; Tian, C. Wang, J.; Yue, X.; Zhang, L. Ma, Effect of potassium promoter on Fischer-Tropsch synthesis to light olefins over iron carbide catalysts encapsulated in graphene-like carbon, Catal. Sci. Technol. 9 (11) (2019) 2728–2741, https://doi.org/10.1039/C9CY00403C.

[53] Y.; Cheng, J.; Lin, K.; Xu, H.; Wang, X.; Yao, Y.; Pei, S.; Yan, M.; Qiao, B. Zong, Fischer-Tropsch synthesis to lower olefins over potassium-promoted reduced graphene oxide supported iron catalysts, ACS Catal. 6 (1) (2016) 389–399. https://pubs.acs.org/doi/10.1021/acscatal.5b02024.

[54] J.; Zhu, M.; Mu, Y.; Liu, M.; Zhang, G.; Zhang, Z.; Cheng, B.; Yin, A.C.K. Yip, C. Song, X. Guo, Unveiling the promoting effect of potassium on the structural evolution of iron catalysts during CO_2 hydrogenation, Chem. Eng. Sci. 282 (2023) 119228, https://doi.org/10.1016/j.ces.2023.119228.

[55] R.; Satthawong, N.; Koizumi, C.; Song, P. Prasassarakich, Bimetallic Fe-Co catalysts for CO_2 hydrogenation to higher hydrocarbons, J. CO_2 Util. 3-4 (2013) 102–106, https://doi.org/10.1016/j.jcou.2013.10.002.

[56] H.; Raghav, C.; Pendem, S.; Tripathi, S.; Kumar, B. Sarkar, Enhanced light olefin production from CO_2 over potassium promoted Fe-Co bimetallic ZrO_2 supported catalysts, Fuel 368 (2024) 131645, https://doi.org/10.1016/j.fuel.2024.131645.

[57] S.; Wang, Y.; Ji, X.; Liu, S. Yan, S.; Xie, Y.; Pei, H.; Li, M.; Qiao, B. Zong, Potassium as a versatile promoter to tailor the distribution of the olefins in CO_2 hydrogenation over iron-based catalyst, ChemCatChem 14 (2022) e202101535, https://doi.org/10.1002/cctc.202101535.
[58] Z.; You, W.; Deng, Q.; Zhang, Y. Wang, Hydrogenation of carbon dioxide to light olefins over non-supported iron catalyst, Chin. J. Catal. 34 (5) (2013) 956–963, https://doi.org/10.1016/S1872-2067(12)60559-2.
[59] A.; Fedorov, H.; Lund, V.A. Kondratenko, E.V. Kondratenko, D. Linke, Elucidating reaction pathways occurring in CO_2 hydrogenation over Fe-based catalysts, Appl. Catal. B Environ. 328 (2023) 122505, https://doi.org/10.1016/j.apcatb.2023.122505.
[60] W. Meng, B.C.A. de Jong, H. Bovenkamp, G. Boer, G.L. Bezemer, A.I. Dugulan, J. Xie, Selectivity control between reverse water-gas shift and Fischer-Tropsch synthesis in carbon-supported iron-based catalysts for CO_2 hydrogenation, CEJ 489 (2024) 151166, https://doi.org/10.1016/j.cej.2024.151166.
[61] J. Liu, P. Wang, W. Xu, E.J.M. Hensen, Particle size and crystal phase effects in Fischer-Tropsch catalysts, Eng 3 (2017) 467–476, https://doi.org/10.1016/J.ENG.2017.04.012.
[62] W. Ma, A.K. Dalai, Effects of structure and particle size of iron, cobalt and ruthenium catalysts on Fischer-Tropsch synthesis, Reactions 2 (2021) 62–77, https://doi.org/10.3390/reactions2010006.
[63] G.C. Bond, The origins of particle size effects in heterogeneous catalysis, Surf. Sci. 156 (1985) 2, https://doi.org/10.1016/0039-6028(85)90273-0.
[64] L.; Dai, Y.; Chen, R.; Liu, X. Li, N.; Ullah, Z. Li, CO_2 hydrogenation to C_{5+} hydrocarbons over K-promoted Fe/CNT catalyst: Effect of potassium on structure-activity relationship, Appl. Organomet. Chem. 35 (2021) e6253, https://doi.org/10.1002/aoc.6253.
[65] J.; Zielinski, I. Zglinicka, L.; Znak, Z. Kaszkur, Reduction of Fe_2O_3 with hydrogen, Appl. Catal. A Gen. 381 (2010) 191–196, https://doi.org/10.1016/j.apcata.2010.04.003.
[66] L.; Niu, X.; Liu, X.; Wen, Y.; Yang, J. Xu, Y. Li, Effect of potassium promoter on phase transformation during H_2 pretreatment of a Fe_2O_3 Fischer Tropsch synthesis catalyst precursor, Catal. Today 343 (2020) 101–111, https://doi.org/10.1016/j.cattod.2019.01.054.
[67] Y.; Wei, D.; Luo, C.; Zhang, J.; Liu, Y.; He, X.; Wen, Y.; Yang, Y. Li, Precursor controlled synthesis of graphene oxide supported iron catalysts for Fischer-Tropsch synthesis, Catal. Sci. Technol. 8 (2018) 2883–2893, https://doi.org/10.1039/C8CY00617B.
[68] J.; Liu, Y.; Zhang, C. Peng, Recent advances hydrogenation of carbon dioxide to light olefins over iron-based catalysts via the Fischer-Tropsch synthesis, ACS Omega 9 (24) (2024) 25610–25624, https://doi.org/10.1021/acsomega.4c03075.
[69] X.; Chen, R.; Gao, Q. Wang, K.; Hu, F. Wang, C. Deng, L.; Xu, C.; Zhang, K.W.; Jun, S.K.; Kim, T.; Zhao, H.; Wan, G. Guan, Direct hydrogenation of CO_2 to liquid hydrocarbons over K/Fe-C catalysts: Effect of porous carbon matrix and K modification, Fuel 364 (2024) 131061, https://doi.org/10.1016/j.fuel.2024.131061.
[70] K.; Qin, Y.; Men, S.; Liu, J.; Wang, Z.; Li, D.; Tian, T.; Shi, W.; An, X.; Pan, L. Li, Direct conversion of carbon dioxide to liquid hydrocarbons over K-modified $CoFeO_x$/zeolite multifunctional catalysts, J. CO_2 Util. 65 (2022) 102208, https://doi.org/10.1016/j.jcou.2022.102208.